Charge carrier complexes in monolayer semiconductors

E. Mostaani,[1] R. J. Hunt,[2,3] D. M. Thomas,[2] M. Szyniszewski,[2,4] A. R.-P. Montblanch,[5] M. Barbone,[1,5] M. Atatüre,[5] N. D. Drummond,[2] and A. C. Ferrari[1]

[1]*Cambridge Graphene Centre, University of Cambridge, 9 J. J. Thomson Avenue, Cambridge CB3 0FA, United Kingdom*
[2]*Department of Physics, Lancaster University, Lancaster LA1 4YB, United Kingdom*
[3]*Department of Engineering, Lancaster University, Lancaster LA1 4YB, United Kingdom*
[4]*Department of Physics and Astronomy, University College London, London WC1E 6BT, United Kingdom*
[5]*Cavendish Laboratory, University of Cambridge, 19 J. J. Thomson Avenue, Cambridge CB3 0HE, United Kingdom*

(Received 4 September 2022; revised 9 May 2023; accepted 8 June 2023; published 26 July 2023)

The photoluminescence (PL) spectra of monolayer (1L) semiconductors feature peaks ascribed to different charge-carrier complexes. We perform diffusion quantum Monte Carlo simulations of the binding energies of these complexes and examine their response to electric and magnetic fields. We focus on quintons (charged biexcitons), since they are the largest free charge-carrier complexes in undoped and low doping transition-metal dichalcogenides (TMDs). We examine the accuracy of the Rytova-Keldysh interaction potential between charges by comparing the binding energies (BEs) of charge-carrier complexes in 1L-TMDs with results obtained using *ab initio* interaction potentials. Magnetic fields <8 T change BEs by ~ 0.2 meV T^{-1}, in agreement with experiments, with BE variations of different complexes being very similar. Our results will help identify charge complexes in the PL spectra of 1L semiconductors.

DOI: 10.1103/PhysRevB.108.035420

I. INTRODUCTION

The optical properties of layered semiconductors, such as transition-metal dichalcogenides (TMDs), change as the sample thickness is reduced from bulk (B) to a single layer (1L) [1]. Indirect band gaps in B-TMDs are often observed to transition to direct ones in 1L [2], accompanied by the emergence of photoluminescence (PL) [3]. Excitonic effects are enhanced in 1L relative to B-TMDs, due to reduction in electrostatic screening of the interactions between charge carriers [4]. In many 1L semiconductors, including TMDs with honeycomb lattices, spin-orbit coupling splits the conduction (CB) and valence (VB) bands at their extrema at the K and K' points of the Brillouin zone [5–7]. This results in optically controllable spin and valley degrees of freedom [8–10]. Valley polarization is retained for >1 ns [8,11], ideal for quantum device applications, such as quantum light-emitting diodes [12–15]. Localized single-photon emitters that can be controlled by electroluminescence [12,15] are also promising for quantum photonics [15].

The binding energy (BE) of an exciton may be calculated from first principles by solving the Bethe-Salpeter equation (BSE) [16] on top of many-body perturbation theory calculations within the *GW* approximation [17–19], or by quantum Monte Carlo (QMC) methods [20]. However, studying charge-carrier complexes, such as quintons, using these approaches is computationally expensive [21]. Instead, the effective-mass approximation [22] can be used, whereby the ground-state energy is modelled by considering an electron (e) and a hole (h) interacting within a two-band model [23], and their effective masses are defined by experiment, or by first principles band structure calculations. In effective-mass models of charge-carrier complexes in layered semiconductor materials (LSMs), it is crucial to take into account the two-dimensional (2d) nature of the electrostatic screening, as this modifies the form of the interaction between carriers [24,25]. The situation for LSMs differs from III-V semiconductor heterostructures with a thickness>1 μm [26], in which the Coulomb $1/r$ interaction between charge carriers scales down with the permittivity of the host material [26]. In LSMs, the so-called Rytova-Keldysh interaction (RKI) potential [24,25] provides a more accurate interaction between charge carriers. References [27–29] studied the formation of multicarrier bound states in 1L-LSMs using QMC methods, such as path integral Monte Carlo [30] and diffusion Monte Carlo (DMC) [21] to solve the Schrödinger equation for quasiparticles interacting via the RKI potential. DMC is particularly powerful in studies of complexes with distinguishable quasiparticles [31], as it is numerically exact in this case [32]. Reference [29] used DMC to predict the stability of negative quintons in TMDs with distinguishable charge carriers (in which all three e species have different spin and/or valley degrees of freedom). These predictions were confirmed in experimental studies, which provided evidence of quintons in hBN-encapsulated 1L-WSe_2 [33–36], 1L-$MoSe_2$ on sapphire [37], and 1L-WSe_2 on Si/SiO_2 [38].

In Mo and W-TMDs, the VB spin-splitting is sufficiently large that the lower spin-split bands are always occupied at room temperature (RT) [7], while the CB spin-splitting is comparable with RT [7]. As a result, there are effectively 4 e

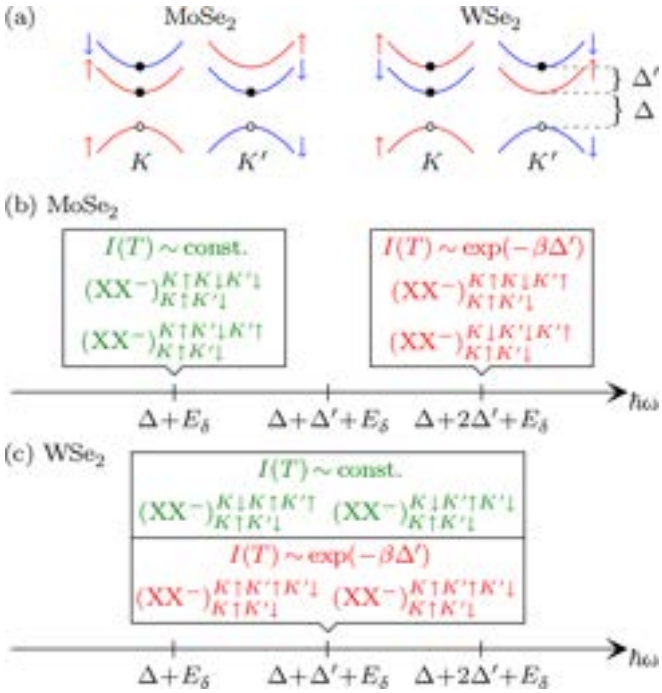

FIG. 1. (a) Upper spin-split VB and spin-split CB for 1L-$MoSe_2$ and 1L-WSe_2. The spin-split VB is >150 meV [7], so we only show the upper VB. [(b) and (c)] Classification of quinton recombination processes in 1L-Mo and 1L-W-TMDs. $E_\delta = E_{XX^-} - E_{X^-}$ is the difference between the total energies E_{XX^-} and E_{X^-} of XX^- and X^-. $\hbar\omega$ indicates the photon energies at which XX^- peaks in PL spectra are expected. $(XX^-)^{k_1\sigma_1 k_2\sigma_2 k_3\sigma_3}_{k_4\sigma_4 k_5\sigma_5}$ denotes a quinton consisting of CB e in valleys k_1, k_2, and k_3 with spins σ_1, σ_2, and σ_3 and VB h in valleys k_4 and k_5, with spins σ_4 and σ_5. For example, the quintons in (a) are both $(XX^-)^{K\uparrow K\downarrow K'\downarrow}_{K\uparrow K'\downarrow}$. Unlike Figs. 1 and 2 of Ref. [29], we only show complexes with distinguishable charge carriers, because they are stable and should be experimentally observable. Note that in (b) recombination may be followed by momentum exchange, giving an additional contribution of $2\Delta'$.

and 2 h species available to form charge-carrier complexes at and below RT [29]. We consider all quasiparticles in quintons to be distinguishable, because in TMDs, e.g., they comprise 3 e and 2 h species distinguishable due to their different spin and/or valley degrees of freedom, as shown in Fig. 1(a). The reason why 2 of the 3 e are not considered as indistinguishable is that, with 2 available valleys in the CB [7], and 2 spins [7], and a spin-orbit splitting of the CB comparable to RT [7], there are effectively 4 available e species in TMDs [7]. Quintons have 3 e distinguishable by valley and spin degree of freedom, as shown in Fig. 1(a), because they can occupy 3 of 4 available distinguishable levels. A biexciton with 2 indistinguishable e is unstable except at extreme mass ratios ($m_e/m_h > 3$), because exchange effects between the heavy particles are negligible, as shown in Ref. [29]. Adding 1 e to form a quinton will make the complex even less stable, because the size of the charge complex increases. Hence, we consider only the case of distinguishable e.

One can distinguish dark [39,40], bright [39,41], and semidark [42] charge-carrier complexes in TMDs. In dark complexes, Figs. 2(a) and 2(b), radiative e-h recombination is not allowed due to spin and/or momentum mismatch between the constituent e/h [43], while in bright complexes, Fig. 2(c), direct radiative e-h recombination is allowed by conservation of linear and angular momentum [44]. In semidark complexes, Fig. 2(d), radiative recombination can take place following an intervalley scattering event assisted by a phonon that maintains spin, but swaps an e, e.g., from valley K' to K [40–42,45], accompanied by an energy shift due to the change in occupation of the upper and lower spin-split bands [42].

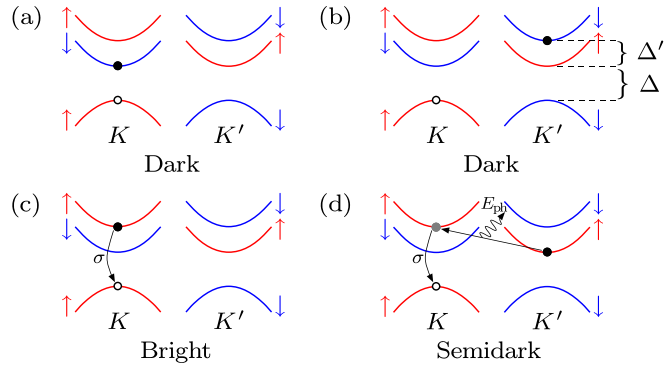

FIG. 2. Classification of e-h recombination processes, showing examples of [(a) and (b)] dark excitons, where recombination is prohibited, (c) bright excitons, where recombination is allowed, and (d) semidark excitons, where recombination is assisted by phonon emission/absorption E_{ph}.

Due to the nature of the CB spin-splitting of Mo-TMDs [7,46–48], Fig. 1(a), bright states are energetically lower than dark [46,49,50]. Hence, at low temperature $T < 100K$, e in exciton (X), negative trion (X^-), and biexciton (XX) complexes occupy the lower spin-split bands. X complexes therefore travel only a small distance, e.g., ~1 μm in 1L-Mo-TMDs [51,52], before radiative recombination, which reduces the chance to bind with another charge-carrier complex [53]. Furthermore, the XX PL peak may be difficult to distinguish from that of X^-, due to the small energy difference ~10 meV between their BEs [51]. Reference [37] detected XX and quintons (XX^-) in 1L-$MoSe_2$ by 2d coherent spectroscopy (2dCS) [54]. This method can focus on a delay time~10 ps, over which XX or XX^- are likely to form [55,56]. However, in 1L-W-TMDs, the most energetically stable excitonic states are dark [49], so that X have longer lifetimes (~1 ps) [49] than in 1L-Mo-TMDs (~0.5 ps) [49], favoring larger than X complexes. We thus focus on 1L-W-TMDs when comparing theory with experiments.

Figure 1 classifies XX^- in 1L-Mo- and W-TMDs with respect to recombination energy and T-dependence of the emitted photons' intensity. There are two XX^- types: (1) those with 1e in the upper spin-split CB and 2e in the lower spin-split CB, and (2) those with 2e in the upper spin-split CB and 1e in the lower spin-split CB. The CB spin splittings in 1L-Mo- and W-TMDs are ~3 and ~30 meV [7], respectively. These are much less than the XX^- BEs ~50 meV [33,37,57], as reported in Table I. The fact that the XX^- BE is larger than the spin splitting implies XX^- complexes are thermodynamically stable at T close to 0 K, even taking into account the energy required to excite 1e to the upper spin-split CB. Assuming the CB spin-orbit splitting Δ' of 1L-TMDs to be $\ll$ XX^- BE, $E^b_{XX^-}$, each XX^- can be treated as a two-state

TABLE I. $E^{b}_{XX^-}$ of XX^- calculated by DMC and by Eq. (7), compared with experiments from Refs. [33,37,38,57]. The e and h effective masses m_e and m_h in terms of the free e mass m_0 are taken from many-body *GW* calculations [17,61]. We assume the materials suspended in vacuum, or encapsulated in hBN, or placed on top of a substrate such as SiO_2 [38] and sapphire [37]. Wherever $\epsilon \neq \epsilon_0$, the vacuum r_* is used. All e and h are considered distinguishable.

TMD	$\frac{m_e}{m_0}$	$\frac{m_h}{m_0}$	ϵ	Vacuum r_* (Å)	BE of XX^- ($E^{b}_{XX^-}$) (meV) DMC	Eq. (8)	Experiment
1L-MoS_2 (vac.)	0.35	0.428 [5]	ϵ_0	38.62 [5]	58.6(6)	59.33	
1L-$MoSe_2$ (vac.)	0.38	0.44 [62]	ϵ_0	39.79 [63]	57.0(4)	58.13	
1L-$MoSe_2$(sapph. subs.)	0.38	0.44 [62]	ϵ_0	52.2 [a]		46.1	$\sim$ 40 [37]
	0.38	0.44 [62]	$4.95\epsilon_0$	39.79 [63]		29.3	
1L-$MoTe_2$ (vac.)	0.65	0.64 [61]	ϵ_0	73.61 [64]	33.8(3)	35.61	
1L-WS_2 (vac.)	0.27	0.32 [62]	ϵ_0	37.89 [65]	57.4(3)	57.60	
1L-WS_2(hBN)	0.27	0.32 [62]	ϵ_0	45.1 [b]		49.7	52.4 [57]
	0.27	0.32 [62]	$4\epsilon_0$	37.89 [65]		31.4	
1L-WSe_2 (vac.)	0.29	0.34 [62]	ϵ_0	45.11 [65]	52.0(7)	50.23	
1L-WSe_2(SiO_2 subs.)	0.29	0.34 [62]	ϵ_0	44.33 [c]		50.97	51 [38]
	0.29	0.34 [62]	$2.45\epsilon_0$	45.11 [65]		37.6	
1L-WSe_2 (hBN)	0.29	0.34 [62]	ϵ_0	48 [d]		47.7	49 [33], 50.7 [57]
	0.29	0.34 [62]	$4\epsilon_0$	45.11 [65]		28	
1L-WTe_2 (vac.)	0.325	0.460 [7]	ϵ_0	49.56 [63,66]	47.5(3)	48.56	

[a]The experimental XX and X^- BEs are $\sim$18 and $\sim$27 meV [37], respectively. With $r_* = 52.2$ Å and $\epsilon = \epsilon_0$, Eqs. (48) and (49) of Ref. [29] give XX and X^- BEs $\sim$17.9, 27.6 meV, respectively.
[b]The experimental XX and X^- BEs are $\sim$19.2 and $\sim$30.2 meV [57], respectively. With $r_* = 45.1$ Å and $\epsilon = \epsilon_0$, Eqs. (48) and (49) of Ref. [29] give XX and X^- BEs $\sim$19.9, 29.2 meV, respectively.
[c]The experimental X^- BE is $\sim$30 meV [38]. With $r_* = 44.33$ Å and $\epsilon = \epsilon_0$, Eq. (49) of Ref. [29] gives BE $\sim$ 30 meV.
[d]The experimental XX BEs are $\sim$18.2 meV [33] or $\sim$20.1 meV [57], and those of X^- are $\sim$27.1 meV [33] or $\sim$29.7 meV [57]. With $r_* = 48$ Å and $\epsilon = \epsilon_0$, Eqs. (48) and (49) of Ref. [29] give XX and X^- BEs $\sim$18.9, 28.1 meV, respectively.

system [58]. For $k_B T \ll \Delta' \ll E^{b}_{XX^-}$, with k_B the Boltzmann's constant, the fraction of XX^- with 1e and 2e in the upper spin-split CB, hence the PL intensity of the corresponding XX^-, is:

$$I(T) \sim \begin{cases} \text{const.} & \text{for 1 e in upper spin band} \\ e^{-\Delta'/(k_B T)} & \text{for 2 e in upper spin band} \end{cases} \quad (1)$$

Here, we use DMC within the effective-mass approximation to calculate XX^- energies in 1L-LSMs. XX^- are the largest free charge-carrier complexes in TMDs [29] at dilute limit (electron density $< 1.5 \times 10^{12}\,\text{cm}^{-2}$). In highly doped TMDs, larger charge-carrier complexes, such as six and eight body states, may form [59]. We provide an interpolation formula for XX^- BEs for all 1L-LSMs as a function of e and h effective masses, permittivity of the surrounding media, and in-plane susceptibility of the 1L-LSM. We also use DMC to calculate the energies of charge-carrier complexes in the presence of out-of-plane magnetic and in-plane electric fields. Our studies of charge-carrier complexes in external fields help understand and identify them, e.g. in experimental PL spectra of TMDs. This helps to identify whether the behavior in external fields can be used to investigate PL peaks. We find that applying an external magnetic field helps identifying charge-carrier complexes in 1L-LSMs with different e and h effective masses, while electric fields can be used to identify charge-carrier complexes in all 1L-LSMs. We explore the accuracy of the RKI potential by comparing BEs with results obtained using *ab initio* random-phase approximation (RPA) interaction potentials [60]. We find that, within the effective-mass approximation, RKI can describe quasiparticles on length scales larger than the lattice constant. Thus, our results can be used to determine the PL of excitonic complexes.

II. RESULTS AND DISCUSSION

A. Units

In the following, we will use Hartree excitonic units (e.u.), in which the e-h reduced mass μ, 4π times the absolute permittivity ϵ, the Dirac constant $\hbar$, and the charge e are all equal to 1, i.e., $\mu = 4\pi\epsilon = \hbar = e = 1$. This helps to scale the BEs with respect to r_* and effective masses, as explained in Methods. The screening length is $r_* \equiv \kappa/(2\epsilon)$, with κ the in-plane susceptibility, as discussed in Methods. The e.u. of length is the exciton Bohr radius $a_0^* = 4\pi\epsilon\hbar^2/(\mu e^2)$ [67], that of magnetic flux density is $B^* = \mu^2 e^3/[(4\pi\epsilon)^2\hbar^3]$, that of electric field is $F^* = \mu^2 e^5/[(4\pi\epsilon)^3\hbar^4]$, and that of energy is the exciton Hartree $2R_y^*$, with $R_y^* = \mu e^4/[2(4\pi\epsilon)^2\hbar^2]$ the exciton Rydberg constant [67].

For the logarithmic approximation to the RKI we will use a different set of units, as explained in Ref. [29]. Since in the logarithmic regime $r \ll r_*$, where r is the separation between charge carriers, the behavior of the energy changes when compared with the intermediate regime $r \gg r_*$. In the logarithmic e.u., the e-h reduced mass μ, $4\pi\epsilon r_*$, $\hbar$, and the electronic charge are all equal to 1, i.e., $\mu = 4\pi\epsilon r_* = \hbar = e = 1$. We define the logarithmic e.u. of length to be $\sqrt{2}r_0$, where $r_0 = \sqrt{4\pi\epsilon r_*\hbar^2/(2e^2\mu)}$, the unit of energy $E_0 = e^2/(4\pi\epsilon r_*)$, the unit of magnetic flux density $B_0 = \sqrt{\mu E_0}/(\sqrt{2}er_0) = e\mu/(4\pi\epsilon r_*\hbar)$, and the unit of electric field $F_0 = E_0/(\sqrt{2}r_0 e) = \sqrt{e^4\mu/[(4\pi\epsilon r_*)^3\hbar^2]}$.

To convert the Bohr radius, flux density, electric field, and energy from e.u. to SI units, each value needs to be multiplied by a_0^*, B^*, F^*, and $2R_y^*$, respectively. To convert from logarithmic e.u. to SI units, each value needs to be multiplied by $\sqrt{2}r_0$, B_0, F_0, and E_0, respectively.

Table II summarizes all acronyms in this paper [68].

B. Binding energies

We define the X, X^-, and XX BEs as:

$$E_X^b = E_e + E_h - E_X, \tag{2}$$

$$E_{X^-}^b = E_e + E_X - E_{X^-}, \tag{3}$$

$$E_{XX}^b = 2E_X - E_{XX}, \tag{4}$$

where the complexes are defined in Table II. In the absence of external fields, $E_e = E_h = 0$.

We define the de-excitonization energy of XX^- as:

$$E_{XX^-}^{DE} = E_X + E_{X^-} - E_{XX^-}, \tag{5}$$

and the electron affinity of XX as:

$$\begin{aligned} E_{XX}^{EA} &= E_{XX} + E_e - E_{X^-} \\ &= E_{X^-}^b - E_{XX}^b + E_{XX^-}^{DE}. \end{aligned} \tag{6}$$

Since the most stable dissociated complexes have the lowest ground-state energies, the XX^- BE is the minimum of $E_{XX^-}^{DE}$ and E_{XX}^{EA} for a given r_* and effective mass:

$$E_{X^-}^b = \min\left\{E_{XX}^{EA}, E_{XX^-}^{DE}\right\}. \tag{7}$$

Comparing Eq. (7) with Eqs. (5) and (6) for 1L-TMDs, the energy difference between bright X and XX^- PL peaks is $E_{XX^-}^{DE}$.

We calculate $E_{XX^-}^{DE}$ of XX^- complexes in all 1L-LSMs with all possible values for $r_*/a_0^* = \{0, 0.5, 1, 2, 4, 6, 8, \infty\}$ and $\sigma = \{0, 0.1, 0.2, \ldots, 1, 1.5, 4, 9, \infty\}$, where $\sigma = m_e/m_h$ is the mass ratio. We fit:

$$\frac{E_{XX^-}^{DE}}{R_y^*(1-y)} = \frac{\sum_{i=0}^{4}\sum_{j=0}^{5-i} a_{ij}x^i y^j + b_1\sqrt{x} + b_2\sqrt{1-x}}{1 + \sum_{k=1}^{3} c_k y^k + y^2(d_1\sqrt{x} + d_2\sqrt{1-x})} \tag{8}$$

to our DMC $E_{XX^-}^{DE}$, where $\{a_{ij}\}$, $\{b_i\}$, $\{c_i\}$, and $\{d_i\}$ are fitting parameters, $x = \sigma/(\sigma+1) = m_e/(m_e+m_h)$ is a rescaled mass ratio and $y = r_*/(r_* + a_0^*)$ a rescaled in-plane susceptibility parameter. The fitting function goes as the square root of the mass at extreme mass ratios ($\sigma = 0$ and $\sigma = \infty$), as required by the Born-Oppenheimer approximation [67]. We fit $E_{XX^-}^{DE}/[R_y^*(1-y)]$ so that the asymptotic behavior at $r_* \to \infty$

TABLE II. List of acronyms

Symbol	Definition
	General acronyms
2d	two-dimensional
TMD	Transition metal dichalcogenide
1L	Monolayer
ML	Multilayer
LSMs	Layered semiconductor materials
RT	Room temperature
BE	Binding energy
VB	Valence band
CB	Conduction band
PL	Photoluminescence
e.u.	Hartree excitonic units
SI	International system
μ	Reduced mass
m_e	Electron effective mass
m_h	Hole effective mass
m_0	Free electron mass
CoM	Center of mass
ϵ	Absolute permittivity
$\hbar$	Dirac constant
r_*	Screening length
B	Magnetic flux density
F	Electric field
R_y^*	Exciton Rydberg constant
a_0^*	exciton Bohr radius
	Charge complexes
e, h	Single electron, single hole
X	Exciton
X^-	Negative trion (negatively charged exciton)
X^+	Positive trion (positively charged exciton)
XX	Biexciton (bound states of 2e and 2h)
XX^-	Quinton (bound states of 3e and 2h)
D^-XX	Donor-bound double-negative biexciton
D^0X^-	Donor-bound double-negative exciton
	Total energies
E_e	Ground-state total energy of electron
E_h	Ground-state total energy of hole
E_X	Ground-state total energy of exciton
E_{X^-}	Ground-state total energy of negative trion
E_{XX}	Ground-state total energy of biexciton
E_{XX^-}	Ground-state total energy of quinton
	Binding energies
E_X^b	Binding energy of exciton
$E_{X^-}^b$	Binding energy of negative trion
E_{XX}^b	Binding energy of biexciton
$E_{XX^-}^b$	Binding energy of quinton
$E_{XX^-}^{DE}$	Deexcitonization energy of quinton
E_{XX}^{EA}	Electron affinity of biexciton
	Methods
QMC	Quantum Monte Carlo
DMC	Diffusion Monte Carlo
VMC	Variational Monte Carlo
RKI	Rytova-Keldysh interaction
RPA	Random-phase approximation
RPAI	RPA interaction
CW	Continuous wave

obtained using the logarithmic interaction can be included in the fit. The error in the fitted $E^{\rm DE}_{\rm XX^-}$ is $< 5\%$ at each data point. The statistical error bars on the DMC $E^{\rm DE}_{\rm XX^-}$ data points are much smaller than the error in the fit. We therefore use an unweighted least-squares fit [69]. We provide a program [70] that can be used to evaluate $E^{\rm DE}_{\rm XX^-}$ and $\rm XX^-$ BE for any 1L-LSM, for which effective masses, r_*, and dielectric constant of the environment are the inputs.

Using the BE fits in Eqs. (48) and (49) of Ref. [29] together with Eqs. (6)–(8), we calculate the $\rm XX^-$ BEs in Fig. 3. Above the yellow line in Fig. 3(c), the $\rm XX^-$ BE $= E^{\rm DE}_{\rm XX^-}$ (all 1L-TMDs fall in this region). Below the yellow line, the $\rm XX^-$ BE is equal to the XX electron affinity.

Table I lists the $\rm XX^-$ BEs from DMC and the fit of Eq. (8) for 1L-WS_2, 1L-WSe_2, 1L-WTe_2, 1L-MoS_2, 1L-$MoSe_2$, and 1L-$MoTe_2$.

To measure $\rm X^-$, XX, $\rm XX^-$ BEs, in Ref. [33] we used continuous wave (CW) PL at 4K for 1L-WSe_2 encapsulated between two 10 nm (bottom) and 3 nm (top) ML-hBN on Si/SiO_2. Refs. [33,38,57] employed different experimental conditions for 1L-WSe_2, but they all produced similar results, Table I, across various techniques and substrates.

The size of a charge-carrier complex in a 1L-TMD can be defined by r_0. This is $\sim$8 Å for the TMDs listed in Table I, because their e and h masses and screening lengths are around the same order of magnitude. Hence, we suggest that encapsulation in $>$ 1nm ML-hBN can be described by the permittivity $\epsilon = 4\epsilon_0$ [71–75] of bulk hBN.

For ML-hBN-encapsulated TMDs, we test 2 approaches to compare our results with experiments.

(1) We fix $\epsilon = \epsilon_0$ and determine r_* by fitting Eqs. (48) and (49) of Ref. [29] to the experimental $\rm X^-$, XX BEs in Refs. [33,37,38,57]. This is reasonable because, at distances larger than the layer-layer separation, the Keldysh interaction of Eq. (15) for a ML is of the same form as for a 1L [76], but with r_* being the sum of r_* for the different layers [76]. For $r \ll r_*$, only ϵr_* appears in the logarithmic approximation to the Keldysh interaction in Eq. (16), apart from a constant contribution to the total energy, which cancels out of $E^{\rm DE}_{\rm XX^-}$. Hence, it is preferable to fix ϵ, and treat r_* as the independent parameter. The $\rm XX^-$ BEs calculated with this approach for 1L-WSe_2 and 1L-WS_2 encapsulated in ML-hBN agree with the experiments in Refs. [33,57], differing by at most $\sim$ 2 meV, as for Table I.

(2) We use *ab initio* vacuum r_* for 1L-TMDs. To describe hBN encapsulation, we use $\epsilon = 4\epsilon_0$, consistent with Refs. [71–74]. This gives BEs $\sim$ 5–18 meV smaller than Refs. [33,57]. This difference could either be due to the phenomenological parameters (r_* and ϵ), obtained by *ab initio* methods and used in the Mott-Wannier-Keldysh model of Eq. (14), or be a result of neglecting intervalley scattering [77] and contact (exchange) interactions.

The substrate effect on the BE of a charge-carrier complex can be described by:

$$\epsilon = (\epsilon_0 + \epsilon_{\rm substrate})/2, \tag{9}$$

where $\epsilon_{\rm substrate}$ is the bulk permittivity of the substrate. In Ref. [38], 1L-WSe_2 was grown on SiO_2 by physical vapor deposition and the $\rm X^-$ and $\rm XX^-$ BEs of 1L-WSe_2 at

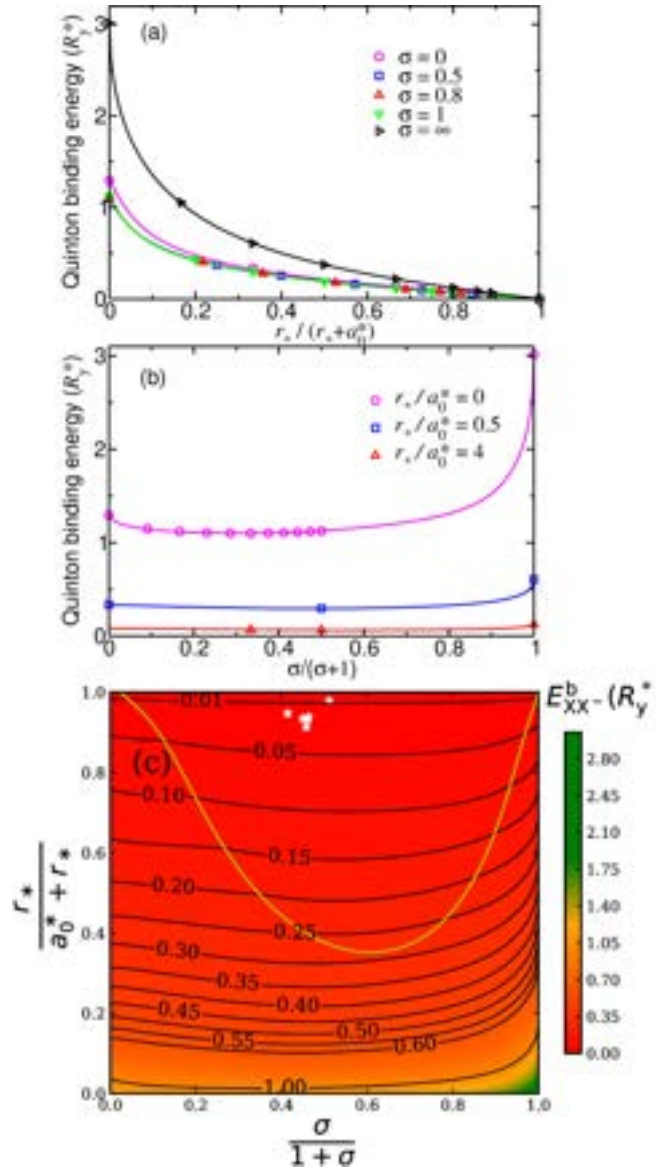

FIG. 3. (a) DMC BEs of $\rm XX^-$ as a function of $r_*/(r_*+a_0^*)$. (b) DMC BEs of $\rm XX^-$ as a function of $\sigma/(\sigma+1)$. (c) $\rm XX^-$ BEs as a function of rescaled susceptibility and mass ratio. Above the yellow line $E^{\rm DE}_{\rm XX^-} <$ XX electron affinity, so that X and $\rm X^-$ are the most energetically competitive. Below the yellow line the situation is reversed, so that XX and free e are the most competitive. The white stars show the mass ratios and in-plane susceptibility of 1L-MoS_2 at (0.45,0.93), 1L-$MoSe_2$ at (0.46, 0.94), 1L-$MoTe_2$ at (0.50,0.98), 1L-WS_2 at (0.46,0.91), 1L-WSe_2 at (0.46,0.93), 1L-WTe_2 at (0.41,0.95), where the first and second numbers in brackets are $\sigma/(\sigma+1)$ and $r_*/(r_*+a_0^*)$, respectively. $\rm XX^-$ BEs are between $0.00736(5)\,R_y^*$ and $0.0288(1)\,R_y^*$, with the numbers in brackets the BE error bars.

RT were measured as $\sim$ 30 and 51meV, respectively, by CW PL. Using the permittivity of SiO_2, $\epsilon_{\rm substrate} \sim 3.9\epsilon_0$ [78] in Eqs. (9) and (8), and Eq. (49) of Ref. [29], we calculate the $\rm X^-$ and $\rm XX^-$ BEs to be $\sim$19 and 38 meV, respectively, $\sim$ 10–13 meV less than the experiments in Ref. [38] done at RT, while our calculations correspond to $T = 0$ K. Approximating the sapphire permittivity as isotropic with $\epsilon_{\rm substrate} = 8.9\epsilon_0$ [79] gives $\rm X^-$, XX, $\rm XX^-$ BEs

in 1L-$MoSe_2$ to be ∼13.6, 13.7, and 30 meV, respectively. We use an effective dielectric constant to describe the environment for 1L-TMDs on a substrate. This is evaluated as the average of the dielectric constants of the media above and below the 1L-TMD. For 1L-TMD on SiO_2, we have SiO_2/TMD/vacuum, hence $\epsilon = \epsilon_0(3.9+1)/2 = 2.45\epsilon_0$. For sapphire/1L-TMD/vacuum, $\epsilon = \epsilon_0(8.9+1)/2 = 4.95\epsilon_0$. In Ref. [37], exfoliated 1L-$MoSe_2$ was transferred to a sapphire substrate and 2dCS at 13 K was used to measure X^-, XX, and XX^- BEs ∼27, 18, and 40meV, respectively [37]. Substrate-induced roughness can also cause inhomogeneity in the electronic structure and extra carrier scattering [80]. This affects PL, leading to inhomogeneous broadening [81,82], which makes it difficult to identify charge-carrier complexes [37]. In Ref. [37], PL spectra were not recorded as a function of excitation power. However, power-dependent measurements help assign the PL peaks to X^-, XX, XX^-, because they show, respectively, sublinear, quadratic, and superlinear dependence with excitation power.

In principle, r_* for encapsulated 1L-TMDs does not depend only on the intrinsic properties of the TMD under investigation, but also on the surrounding dielectric media [76] (and their relative permittivities [76]), and, ultimately, on the electronic structure of the interfacial regions [83] (whose dielectric response arises from their own electronic structure [76]). To simplify calculations, we fix ϵ to the vacuum permittivity and vary r_* as shown in Table I. Due to the complexity in defining r_* and ϵ for 1L-TMDs encapsulated in hBN or placed on a substrate, we use the first approach, where we fix $\epsilon = \epsilon_0$ and determine r_* by fitting theoretical X^- and XX BEs to available experiments, so to define the XX^- BEs. The reason is that calculating the dielectric constant and r_* of encapsulated materials using first-principles requires full understanding of the interfacial and interlayer interactions. Here, we primarily focus on freestanding 1L-LSMs, and then extend our model for encapsulated 1L-LSMs. The components that are missing in the calculations (such as e-h exchange) may be of higher relevance, but the Mott-Wannier model with the Keldysh interaction provides a good description of the energies of excitons, trions, and biexcitons in 1L-LSMs, as discussed in Refs. [28,29,84], and there is no compelling reason to believe that contact interactions should be more important in a quinton than in a trion or biexciton in freestanding 1L-LSMs.

C. Other charge-carrier complexes

We investigate doubly charged complexes, including XX^{2-} (4e and 2h) and D^0hh (one positive donor ion, 1e, 2h), in which all charge carriers are distinguishable. Optimizing wave functions with pairwise and three-body correlations by variational Monte Carlo (VMC) energy minimization [85] does not result in bound-state wave functions. If we constrain the wave function to be bound, and then perform DMC, the resulting energy confirms that complexes are unbound. Thus, doubly charged complexes are unstable for all relevant material parameters at dilute limit (electron density $< 1.5 \times 10^{12}$ cm^{-2}). In highly doped LSMs such complexes may be stable [59].

In Ref. [29] we considered what is the largest stable charge-carrier complex that can occur in 1L-TMDs. We showed that XX with two indistinguishable e are unstable in 1L-TMDs, because of the resulting antisymmetry of the spatial wave function. We concluded that, in bound complexes featuring only singly charged dopant ions and charge carriers, all charge carriers must be distinguishable. Our results show that a charge-carrier complex can feature at most one dopant ion. Because of the band structure [see Fig. 1(a)], 1L-TMDs can have 4e species and 2h species. This suggests that the largest stable cluster will have a positive donor ion, 4 distinguishable e, and 2 distinguishable h. We get bound-state wave functions describing the donor-bound double-negative XX (D^-XX). These seven-body complexes are predicted to be stable in 1L-WS_2, 1L-WSe_2, 1L-MoS_2, 1L-$MoSe_2$ in vacuum and air. The DMC-calculated BEs with respect to the most energetically favorable products [donor-bound negative X (D^0X^-)+free X] are in Table III. Because the dominant decay products include an X, the BE gives the PL peak position of the D^-XX complex relative to the X line, possible in samples containing donor defects.

TABLE III. Theoretical $E^{\rm b}_{\rm D^-XX}$ for 1L-TMDs in vacuum, with *ab initio* masses and r_* from Table I

TMD	$E^{\rm b}_{\rm D^-XX}$ (meV)
1L-MoS_2 (vac.)	58.3(5)
1L-$MoSe_2$ (vac.)	78.6(3)
1L-WS_2 (vac.)	80.4(5)
1L-WSe_2 (vac.)	70.5(7)

D. Accuracy of the Rytova-Keldysh interaction

RKI arises from the approximation that the in-plane susceptibility of a material is a constant [24]. The potential we use is always *ab initio* RPA. *Ab initio* calculations were performed to determine noninteracting band structures of TMDs (via DFT) in Ref. [60], used here, in conjunction with the RPA assumption, to form a dielectric function. We do not have screening of Coulomb interactions by free e (metallic behavior). Instead, we have screening of Coulomb interactions by bound e (insulating/semiconducting behavior). Indeed, at long range ($r \gg r_*$), the potentials we examine reduce to the unscreened Coulomb interaction (or, in the presence of a dielectric environment, to an isotropic, statically screened Coulomb interaction). Here, we investigate the RKI accuracy by using an alternative approach based on *ab initio* calculations for 1L-MoS_2. Realistic dielectric functions exhibit spatial dependencies which differ from the Coulomb interaction at short range ($r \ll r_*$). At long range ($r \gg r_*$), in-plane screening becomes irrelevant, and all physical dielectric functions behave as the Coulomb interaction, as explained in Methods. Given that the binding of excitonic complexes occurs on length scales larger than the lattice spacings (Table I), where screening effects are most prominent (Fig. 4), an investigation into their effects on charge-carrier binding is warranted. Reference [60] parameterized a dielectric permittivity $\epsilon(\mathbf{q})$ for 1L-MoS_2 via RPA applied to Kohn-Sham orbitals from density functional theory calculations to study charged defects. We refer to the real-space interaction formed

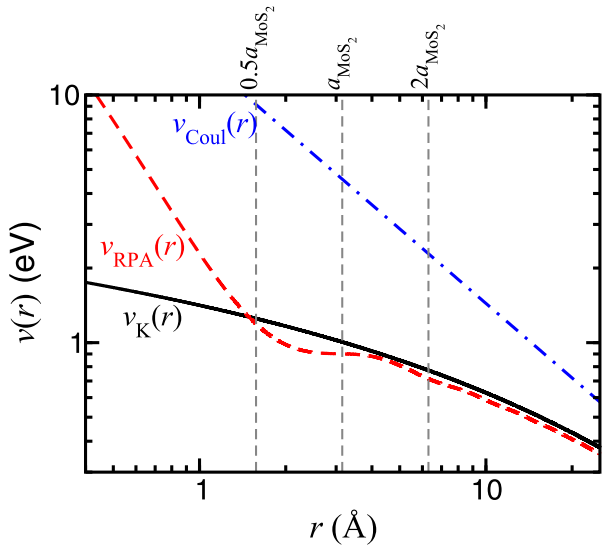

FIG. 4. Unscreened Coulomb interaction potential: $v_{\mathrm{Coul}}(r) = 1/r$; RKI: $v_K(r) = V(r/r_*)/r_*$, with r_* of 1L-MoS_2 in vacuum from Table I; RPAI: $v_{\mathrm{RPA}}(r)$. $a_{\text{1L-MoS}_2} = 3.15$ Å [7].

from $\epsilon(\mathbf{q})$ as the RPA interaction (RPAI), and compare it to RKI in Fig. 4, which plots the potentials in real space.

We use cusp conditions [21] to prevent the wave function of charge carriers to diverge around particle coalescence points [29]. We use the same trial-wave-function form as our calculations with RKI, see Methods for details. As a test, Fig. 5 verifies we reproduce the theoretical donor-atom BEs of Ref. [60], for an adatom-bound e above a 1L-MoS_2 surface. Our data have small $\sim 10^{-4}$–10^{-3} meV error bars, and differ from Ref. [60] by a few meV, for typical BEs $\sim$ a few hundreds meV.

Figure 4 indicates that at distances $> a_{\text{1L-MoS}_2}$, RPAI follows the same form as RKI (and, ultimately, Coulomb) interactions. However, at distances $\sim a_{\text{1L-MoS}_2}$, RKI no longer overlaps RPAI, hence cannot describe the interaction between quasiparticles. Figure 4 shows that for $r \ll 0.5a_{\text{1L-MoS}_2}$, RPAI reduces to an unscreened $1/r$ potential, while the RKI behavior is that of a logarithmic divergence [25]. However, within

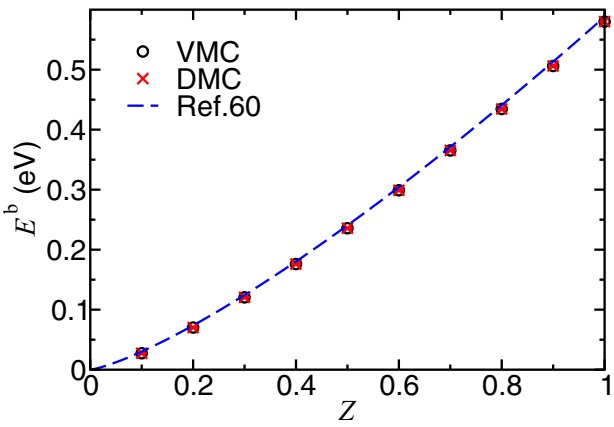

FIG. 5. BE of a donor atom in 1L-MoS_2 as a function of donor impurity charge Z. VMC and DMC results are compared with the numerical data of Ref. [60].

TABLE IV. BEs of charge-carrier complexes in 1L-MoS_2 calculated using different interaction potentials. R-RPA is the rounded RPAI, with r_c in brackets. RKI values from Ref. [29].

	BE (meV)		
Interaction potential	X	X^-	XX
Bare RPA	765.45(2)	77.7(7)	184.5(7)
R-RPA ($2 \times a_{MoS_2}$)	454.5(1)	30.0(3)	16.0(4)
R-RPA (a_{MoS_2})	483.8(4)	30.7(4)	19.4(8)
R-RPA ($0.5 \times a_{MoS_2}$)	492.47(3)	30.9(2)	20.4(4)
RKI	546.5	35.0	23.5
Experiment	~500 [86,87]		
GW-BSE		40.0 [88]	

the effective-mass approximation, we can only describe quasiparticles on length scales $> a_{\text{1L-MoS}_2}$, as shown in Table I and Fig. 4, whose associated Bloch wave packets are localized in momentum space, with well-defined effective mass.

The RPAI BEs of charge-carrier complexes are in Table IV. Removing the bare Coulomb interaction at distances $< a_{\text{1L-MoS}_2}$ is necessary to obtain results in agreement with previous experimental [86,87] and theoretical [88] works. For $r_c < a_{\text{1L-MoS}_2}$, we truncate the RPAI to a constant $v(r < r_c) = v(r_c)$. The precise value of r_c is not particularly important for the BE calculation of charge-carrier complexes, as we observe a weak BE dependence on it, see Table IV.

Table IV indicates that there is no need to use an expression for the electrostatic interaction between charge carriers in LSMs more sophisticated than RKI when evaluating BEs of trions, biexcitons, and quintons. As explained in Methods, any errors in the Mott-Wannier-Keldysh model of charge-carrier complexes for isolated 1L are either due to the parameters (effective masses, r_*, environment permittivity), or to a more fundamental breakdown of the effective-mass approximation. Intervalley scattering may play an important role in the complexes' BEs [60], while exchange effects could be relevant in highly localized complexes [89].

E. Complexes in uniform magnetic fields

For an out-of-plane external magnetic field of flux density $\mathbf{B} = (0, 0, B)$, where B is a positive constant, we can write the Hamiltonian as:

$$\begin{aligned}\hat{H} &= \sum_i \frac{1}{2m_i}(-i\hbar\nabla_i - q_i\mathbf{A}_i)^2 + \sum_{i>j}\frac{q_iq_j}{4\pi\epsilon r_*}V(r_{ij}/r_*)\\ &= \sum_i\left(-\frac{\hbar^2}{2m_i}\nabla_i^2 + i\frac{\hbar q_i}{m_i}\mathbf{A}_i\cdot\nabla_i + \frac{q_i^2|\mathbf{A}_i|^2}{2m_i}\right)\\ &\quad + \sum_{i>j}\frac{q_iq_j}{4\pi\epsilon r_*}V(r_{ij}/r_*),\end{aligned} \tag{10}$$

where $\mathbf{A}_i = -\mathbf{r}_i \times \mathbf{B}/2 = (-y_i, x_i, 0)B/2$ is the magnetic vector potential for particle i in the Coulomb gauge (so that $\nabla_i \cdot \mathbf{A}_i = 0$) [67]. We neglect the charge carriers' intrinsic magnetic dipole moment energy in the external magnetic field, because this contribution cancels out.

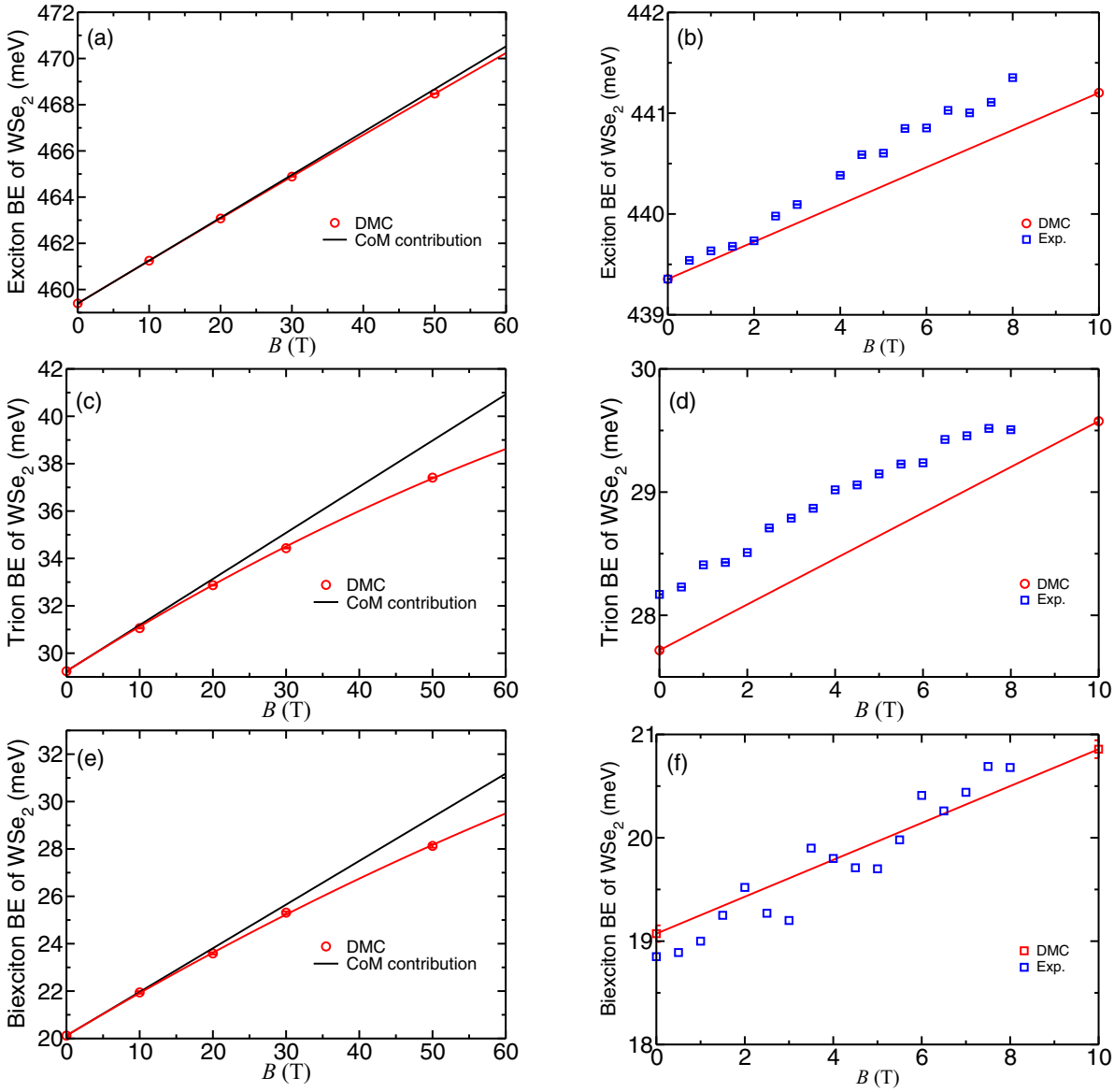

FIG. 6. Theoretical BEs of (a) X, (c) X^-, and (e) XX as a function of perpendicular magnetic field for 1L-WSe_2 in vacuum. We use the *ab initio* mass and r_* parameters of Table I. The CoM contribution for X is $E_X^{b,CoM} = (E_X^b)_{B=0} + E_e + E_h - E_X^{CoM}$; for X^- is $E_{X^-}^{b,CoM} = (E_{X^-}^b)_{B=0} + E_e - E_{X^-}^{CoM}$; and for XX is $E_{XX}^{b,CoM} = (E_{XX}^b)_{B=0} + 2E_X^{CoM} - E_{XX}^{CoM}$. Experimental BEs of (b) X, (d) X^-, (f) XX for 1L-WSe_2 encapsulated in hBN, compared with DMC ones using $\epsilon = \epsilon_0$ and $r_* = 48$ Å and the fit to Eq. (21).

Substituting $\mathbf{A}_i$ into Eq. (10), the term $q_i^2|\mathbf{A}_i|^2/(2m_i) = q_i^2B^2|\mathbf{r}_i|^2/(8m_i)$ provides a quadratic confining potential for the particles in the complex. This cannot be regarded as a perturbation for the (otherwise free) center-of-mass (CoM) motion, because there is a quantitative difference between a bound state wave function in a quadratic potential and free motion in zero potential, no matter how small the quadratic coefficient [31]. The zero-point energy of the CoM motion in the confining potential results in a linear $[O(B)]$ contribution to the total energy, as given in Eq. (12). The term also weakly perturbs the relative motion within the complex, giving a quadratic $[O(B^2)]$ contribution to the energy. We thus include the $q_i^2|\mathbf{A}_i|^2/(2m_i) = q_i^2B^2|\mathbf{r}_i|^2/(8m_i)$ term in our QMC calculations. The linear $(i\hbar q_i/m_i)\mathbf{A}_i \cdot \nabla_i$ term in Eq. (10) breaks time-reversal symmetry as it is imaginary [90]. It only adds to the energy in second-order perturbation theory, giving another $O(B^2)$ contribution. This vanishes when we use a variational Ansatz consisting of a real trial wave function. We therefore neglect it.

The ground-state energies of isolated e/h are $E_e = \hbar eB/(2m_e)$ and $E_h = \hbar eB/(2m_h)$, in the presence of a magnetic field [67]. More generally, if a bound complex of N_e e and N_h h moves in a magnetic field, from Eq. (10) the quadratic confining potential is:

$$U = \sum_i \frac{e^2B^2|\mathbf{r}_i|^2}{8m_i} \approx \frac{B^2e^2}{8}\left(\frac{N_e}{m_e} + \frac{N_h}{m_h}\right)R^2, \qquad (11)$$

where **R** is the CoM position. The total mass of the complex is $N_e m_e + N_h m_h$. Hence, we obtain the CoM zero-point energy of a charge complex as:

$$E^{\mathrm{CoM}} = \frac{\hbar eB}{2}\sqrt{\frac{N_e/m_e + N_h/m_h}{N_e m_e + N_h m_h}}. \tag{12}$$

If $m_e = m_h \equiv m$ then $E^{\mathrm{CoM}} = \hbar eB/(2m)$, independent of N_e, N_h. For a bound complex, our results show that the magnetic field can always be made sufficiently weak so that the external potential is slowly varying on the length scale of the complex (i.e., $\sqrt{\hbar/(eB)} > a_0^*$). Hence, Eq. (12) is the leading-order contribution to the free charge-carrier complex energy in a magnetic field.

Figure 6 plots the DMC X, X^-, XX BEs for 1L-WSe_2 in vacuum, in the presence of an out-of-plane magnetic field, using RKI. m_e, m_h, and r_* are taken from Table I. Our results are in agreement with Ref. [91]. The CoM contribution of Eq. 12 is a good approximation to calculate the X, X^-, XX BEs in magnetic fields <8 T, because it is exact up to linear order in magnetic field, within the effective-mass approximation. For the X BE in magnetic fields > 8 T, we use Eq. (21), derived in Methods. The fitted C in Eq. (21) is 0.557 for X in 1L-WSe_2.

Figures 6(b), 6(d) and 6(f) compare our DMC BEs with measurements for hBN-encapsulated 1L-WSe_2. The sample is produced by exfoliating flux zone grown B-WSe_2 [92], then encapsulating it with ML-hBN (10 nm bottom and 3 nm top) using an all-dry technique [93,94]. Measurements are done in a closed-cycle cryostat (Attocube Attodry 1000) at 4 K, with superconducting magnets allowing out-of-plane magnetic fields up to 8 T. CW excitation is provided with a diode laser at 658 nm, close to the 1L-WSe_2 optical band gap [95]. Polarization-resolved excitation and collection pass through a confocal microscope with the sample in reflection geometry. The PL signal is sent to a liquid-N_2-cooled spectrometer (Princeton).

We assume $r_* = 48$ Å and $\epsilon = \epsilon_0$, as discussed in Sec. II B. The theoretical and experimental BEs differ <0.3 meV over the 0–8 K range. The $O(B)$ magnetic-field dependence is only via the effective masses and N_e, N_h, via the CoM energy, Eq. (12). The fact that the theoretical and experimental magnetic-field trends in Fig. 6 agree well demonstrates that the approximation with *ab initio* effective masses is accurate. The main challenge is to obtain a sufficiently accurate interaction between charge carriers. The BE $O(B)$ term is the same for all complexes, in the limit $m_e = m_h$. For most 1L-TMDs, m_e and m_h are similar, Table I, implying that the magnetic-field dependence cannot be used to distinguish carrier complexes. Table V has DMC and experimental X, X^-, XX BEs for 1L-WSe_2 in the presence of an out-of-plane external magnetic field, as for Fig. 6. The variation of BEs of different charge complexes is the same <8 T.

F. Complexes in uniform electric fields

A bias voltage ΔV applied to a 1L-LSM results in an in-plane electric field. Its precise form depends on device geometry. Here, we assume a uniform electric field $F = -\Delta V/d$, where d is the distance between terminals, for simplicity. F will perturb the energies of charge-carrier complexes in the CoM frame. We therefore investigate the effects of F on BEs by including an additional term $-\sum_i q_i F x_i$ in the Hamiltonian, where x_i is the x coordinate of particle i. Figure 7 plots the X BE shift as a function of electric field strengths for 1L-MoS_2, 1L-$MoSe_2$, 1L-WS_2, 1L-WSe_2, in vacuum and encapsulated by hBN, using the *ab initio* parameters in Table I and $\epsilon = 4\epsilon_0$. In each case, the X BE goes as the square of the in-plane electric field, as expected for a linearly polarizable exciton [96]. Thus the total energy of an isolated neutral complex of polarizability α in a uniform F is:

$$E = E_{F=0} - \alpha F^2/2, \tag{13}$$

where $E_{F=0}$ is the energy of the complex in the absence of external fields. The variation of energy with electric field strength remains quadratic up to at least $\sim 50\ \mathrm{mV\,nm^{-1}}$. At electric fields $> 50\ \mathrm{mV\,nm^{-1}}$ we find that optimizing wave functions by VMC energy minimization does not result in bound-state wave functions. If the parameters in the wave function are fixed such that a bound state is forced, the resulting DMC calculations are unstable. It is possible that some, or all, complexes remain bound at these larger electric fields, and our QMC calculations become unstable, due to the choice of trial wave function. The form we use is isotropic, so it does not allow the complex to polarize in VMC. Polarization arises at DMC level.

TABLE V. DMC and experimental X, X^-, XX BEs in meV for 1L-WSe_2 with an out-of-plane external magnetic field.

	DMC			Experiment		
B (T)	X	X^-	XX	X	X^-	XX
0	439.35	27.72	19.07	439.35	28.17	18.85
1	439.54	27.90	19.25	439.63	28.41	19
2	439.72	28.09	19.43	439.73	28.51	19.52
3	439.91	28.27	19.61	440.09	28.79	19.2
4	440.09	28.46	19.79	440.38	29.02	19.8
5	440.28	28.65	19.96	440.60	29.23	19.7
6	440.46	28.83	20.14	440.85	29.24	20.41
7	440.65	29.02	20.32	441.00	29.46	20.44
8	440.83	29.20	20.5	441.35	29.51	20.68

TABLE VI. Theoretical in-plane polarizabilities of X, XX, D^0, X^-, X^+ in 1L-TMDs, in vacuum and hBN encapsulated

	Polarizability ($\mathrm{eV\,nm^2\,V^{-2}}$)				
TMD	X	XX	D^0	X^-	X^+
1L-MoS_2 (vac.)	5.84(2)	11.14(8)	2.802(9)	66(6)	44(6)
1L-$MoSe_2$ (vac.)	5.76(2)	11.0(1)	2.687(9)	80(9)	45(6)
1L-WS_2 (vac.)	8.04(3)	15.8(1)	3.70(1)	108(10)	72(7)
1L-WSe_2 (vac.)	10.10(4)	24.8(3)	3.96(1)	130(16)	118(9)
1L-MoS_2 (hBN)	17.17(4)	34.2(3)	6.51(2)	179(17)	161(22)
1L-$MoSe_2$ (hBN)	16.22(4)	32.3(2)	6.89(2)	211(22)	181(23)
1L-WS_2 (hBN)	27.16(4)	54.9(3)	4.95(1)	316(27)	246(32)
1L-WSe_2 (hBN)	30.43(4)	61.4(3)	5.29(1)	409(32)	367(32)

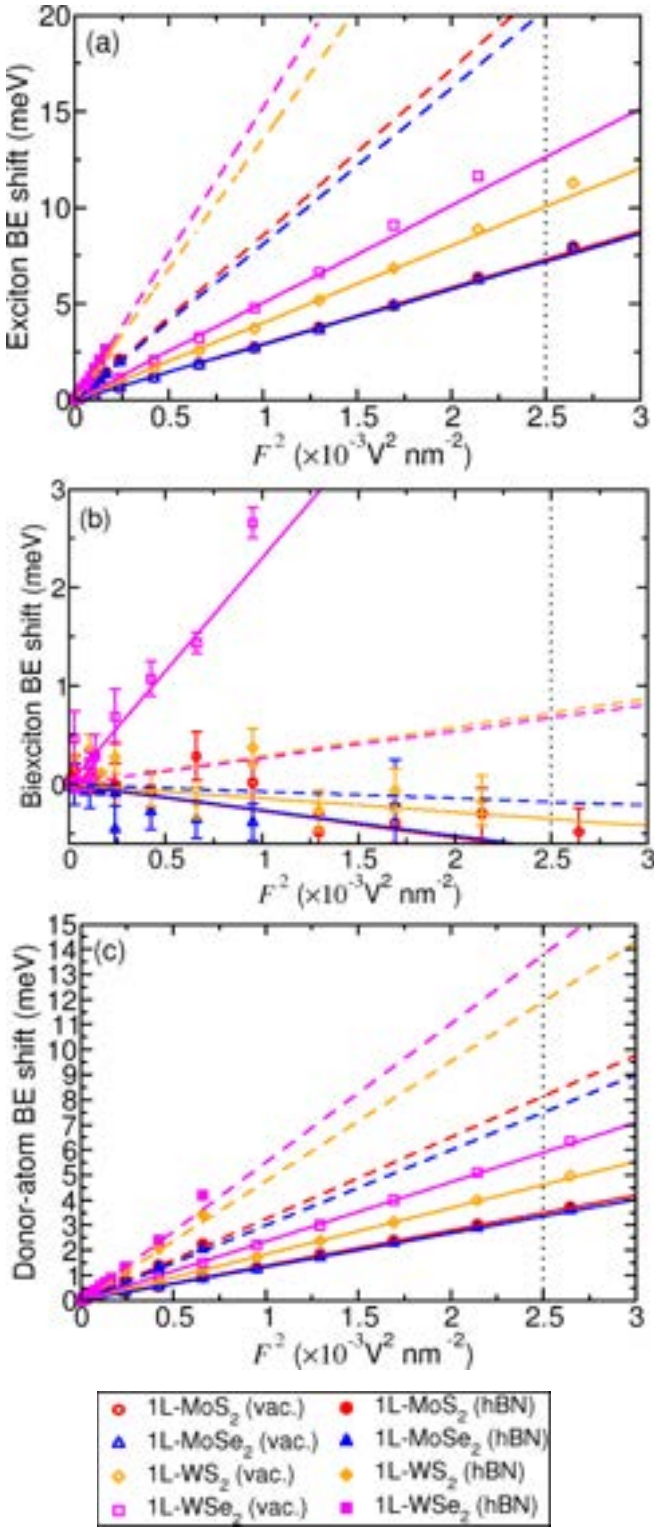

FIG. 7. DMC BE shift for (a) X, (b) XX, (c) donor atoms as a function of F^2 for different 1L-TMDs in vacuum and encapsulated in hBN. Error bars in (a) and (c) are smaller than the symbols. The solid and dashed lines are BEs determined by the polarizabilities in Table VI for 1L-TMDs in vacuum and encapsulated by hBN. The vertical dotted lines correspond to $F = 50$ mV nm^{-1}, beyond which VMC energy minimization does not result in bound-state wave functions.

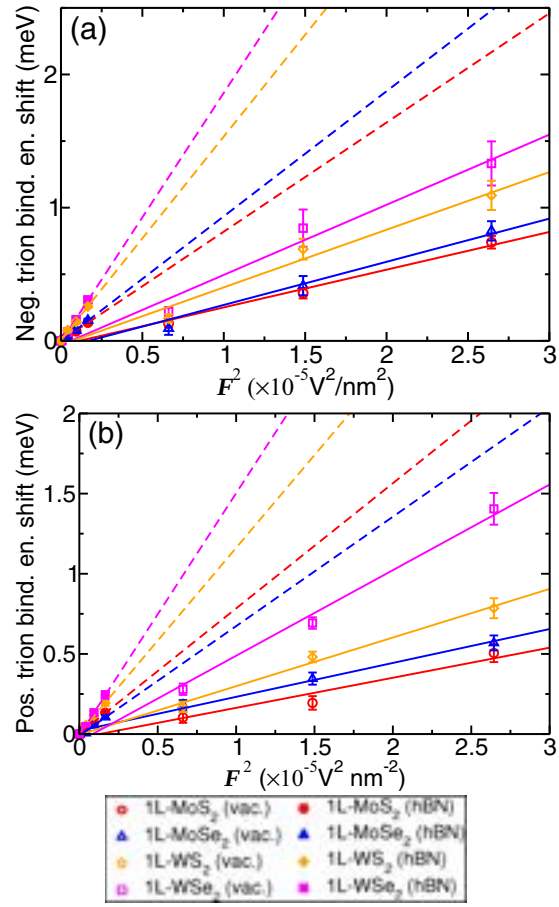

FIG. 8. DMC BE shifts for (a) X^- and (b) X^+ as a function of F^2 for different 1L-TMDs in vacuum and encapsulated in hBN. Where error bars are not visible they are smaller than the symbols. The solid and dashed lines show BEs determined by the polarizabilities in Table VI

The XX and donor-atom BEs vary linearly with F^2, Fig. 7. However, while the donor-atom BEs increase with F^2, the XX BEs decrease. For a 4-particle complex, alignment of charges in the direction of the applied field places like charges closer together, and reduces BE with respect to dissociation into 2-particle complexes. Trion BEs also vary linearly with F^2, Fig. 8. However, QMC calculations become unstable at much lower F. This is reflected in higher polarizabilities for trions than for neutral complexes, Table VI.

The predicted BE shifts of each of the complexes are in Table VII for 1L-TMDs, both in vacuum and encapsulated by hBN, subject to $F = 50$ mV nm^{-1}, beyond which VMC energy minimization does not result in bound-state wave functions. The shifts in the peaks of the trions are so large that, at the very least, they should be experimentally distinguished from the neutral complexes when an electric field is applied. Identification of a positive from a negative trion may be possible in some materials/environments, but not all. For neutral complexes, the differences of a few meV in BE shifts suggest they are unlikely to be experimentally identified by their peak shifts under an electric field.

TABLE VII. Calculated BE shifts of X, XX, D^0, X^-, X^+ using Eq. (13) and polarizabilities in Table VI for 1L-TMDs, both in vacuum and encapsulated by hBN, for $F = 50$ mV nm^{-1}. Not all complexes are bound at $F = 50$ mV nm^{-1}.

	Binding-energy shift (meV)				
TMD	X	XX	D^0	X^-	X^+
1L-MoS_2 (vac.)	7.3	<1	3.5	76	48
1L-$MoSe_2$ (vac.)	7.2	<1	3.4	93	49
1L-WS_2 (vac.)	10.1	<1	4.6	125	80
1L-WSe_2 (vac.)	12.6	5.8	4.9	150	135
1L-MoS_2 (hBN)	21.5	<1	8.1	201	180
1L-$MoSe_2$ (hBN)	20.3	<1	8.6	243	206
1L-WS_2 (hBN)	34.0	<1	6.2	362	273
1L-WSe_2 (hBN)	38.0	<1	6.6	473	408

III. CONCLUSIONS

We used DMC to calculate XX^- BEs in 1L-LSMs within the effective-mass approximation, using the RKI potential. A program available online [70] can be used to evaluate interpolated XX^- BEs given e and h effective masses, in-plane susceptibility, and environment permittivity for a desired 1L-LSM. The BEs of charge-carrier complexes in 1L-LSMs in vacuum from RKI are in excellent agreement with those obtained using interaction potentials taken from *ab initio* RPA, suggesting RKI is a reliable interaction potential to describe screened interaction between charge carriers in 1L-LSMs.

We also considered the effect of external out-of-plane magnetic fields and in-plane electric fields on BEs of charge-carrier complexes in 1L-LSMs. The resulting BE changes are linear in magnetic fields and quadratic in electric fields up to 10 T and 50 mV nm^{-1}.

We measured X, X^-, XX BEs for hBN-encapsulated 1L-WSe_2 up to 8 T, where the BEs vary linearly with magnetic field, and found them to be in good agreement with the effective-mass approximation using *ab initio* effective masses. These BE shifts could in principle be used to identify complexes in PL experiments, provided m_e^* and m_h^* are different. In practice, m_e^* and m_h^* in 1L-TMDs are too similar to distinguish complexes in external magnetic fields. In-plane electric fields should shift the BE peaks in proportion to the field strength and allow for identification of charged from neutral complexes.

We derived BEs of charge-carrier complexes in 1L-TMDs by solving the interacting quantum few-body problem for each complex, working within the effective-mass approximation, with a RKI potential between charge carriers. The BE magnetic-field dependence agrees with experiments on a sub-meV energy scale. Since this only involves m_e^* and m_h^*, and not the parameters describing the screened interaction, the approximation with *ab initio* effective masses is highly accurate.

Efforts to improve the quantitative accuracy of BE calculations should therefore focus on the description of substrate and environmental screening, and on the inclusion of contact interactions and intervalley scattering.

IV. METHODS

A. Effective-mass approximation

All our calculations are performed within the effective-mass approximation. For charge-carrier complexes in 1L-LSMs in the absence of external fields, we solve the Mott-Wannier-Keldysh Schrödinger equation [29]:

$$\left[-\sum_i \frac{\hbar^2}{2m_i}\nabla_i^2 + \sum_{i>j}\frac{q_i q_j}{4\pi\epsilon r_*}V(r_{ij}/r_*)\right]\psi = E\psi, \quad (14)$$

where m_i and q_i are the band effective mass and charge of particle i, r_{ij} is the separation of particles i and j, E is the energy eigenvalue, ϵ is the absolute permittivity of the surrounding medium, and $r_* \equiv \kappa/(2\epsilon)$, where κ is the in-plane susceptibility. In Eq. (14) the electrostatic interaction potential V, known as RKI [24,25,97], is given by [29]:

$$V(r/r_*) = \frac{\pi}{2}[H_0(r/r_*) - Y_0(r/r_*)], \quad (15)$$

where $H_n(x)$ is a Struve function [98] and $Y_n(x)$ is a Bessel function of the second kind [98]. At long range ($r \gg r_*$) the potential in Eq. (15) is a Coulomb interaction $V(r/r_*) \sim r_*/r$; at short range ($r \ll r_*$), logarithmic:

$$V(r/r_*) \approx -\ln\left(\frac{e^\gamma r}{2r_*}\right), \quad (16)$$

where $\gamma \sim 0.57721$ is Euler's constant [98].

We do not include contact interactions between charge carriers due to exchange and correlation effects that occur when they are localized on the same site [89], since these partially cancel out of BEs for complexes larger than X. We consider e to have the same mass in the spin-up and spin-down conduction bands of 1L semiconductors. To test this, we calculate the sensitivity of quinton BEs to the electron mass for 1L-WS_2. We use the h mass as for Table I, but change the spin-down and spin-up e masses to be 10% lighter and 10% heavier than the e mass of 1L-WS_2 in Table I. This is a fair assumption, as Ref. [7] calculated that e in the upper spin-split CBs in 1L-TMDs are $\sim 20\%$ lighter than lower spin-split CBs. Our results show that the quinton binding energy of 1L-WS_2 with different e mass is ~ 59 meV, similar to the ~ 57.4 meV in Table I, also consistent with Table VI of Ref. [29].

B. QMC calculations

We use VMC [85] and DMC [32,99] to calculate the total energies of complexes of charge carriers in 1L-LSMs. We use the RKI potential in Eq. (15) or, for the short range ($r \ll r_*$) limit, the logarithmic interaction of Eq. (16). Our trial wave functions for complexes of distinguishable charge carriers are of the Jastrow form [21], which includes a pairwise sum of terms depending on the distances between charge carriers, as for Ref. [29]. Trial wave functions are optimized within VMC by minimizing first the energy variance [100,101], then the energy expectation [85]. Our fixed-node DMC energies are exact solutions to the Mott-Wannier-Keldysh model of Eq. (14). DMC calculations use time steps in the ratio 1 : 4, with the corresponding target configuration populations in the ratio 4 : 1. The resulting energies are extrapolated linearly to

zero time step and to infinite population. QMC calculations are done with the CASINO code [21].

C. Fitting function for BE as a function of magnetic field

We consider a complex of N_e and N_h e and h interacting via the logarithmic approximation to the Keldysh interaction in the presence of a uniform magnetic field $\mathbf{B} = (0, 0, B)$. Let $\tilde{B} = B/B_0$, $\tilde{m}_i = m_i/\mu$, $\tilde{q}_i = q_i/e$, $\tilde{\mathbf{r}}_i = \mathbf{r}_i/(\sqrt{2}r_0)$, and $\tilde{r}_* = r_*/(\sqrt{2}r_0)$ be magnetic field, mass, charge, and position of particle i. The screening length and the Hamiltonian $\hat{\tilde{H}} = \hat{H}/E_0$ in logarithmic e.u. are as defined in Sec. II A. We thus get:

$$\hat{\tilde{H}} = -\sum_i \frac{1}{2\tilde{m}_i}\tilde{\nabla}_i^2 + \sum_i \frac{\tilde{B}^2\tilde{r}_i^2}{8\tilde{m}_i} - \sum_{i>j}\tilde{q}_i\tilde{q}_j \ln\left(e^\gamma \tilde{r}_{ij}/2\right) + \sum_{i>j}\tilde{q}_i\tilde{q}_j \ln(\tilde{r}_*), \tag{17}$$

where we neglect the term $(i\hbar q_i/m_i)\mathbf{A}_i \cdot \nabla_i$ in Eq. (10) that breaks time-reversal symmetry. The energy eigenvalue $\tilde{E} = E/E_0$ is therefore the sum of a function $f(\sigma, \tilde{B})$, where $\sigma = m_e/m_h$, and an additive constant $c(\tilde{r}_*) = \sum_{i>j}\tilde{q}_i\tilde{q}_j \ln(\tilde{r}_*)$. For X in the absence of an external magnetic field, $\tilde{E}^X_{B=0} = 0.41057747491(7) - \ln(\sqrt{2}) - \ln(\tilde{r}_*)$ was calculated in Ref. [29].

For $\tilde{B}$ such that the magnetic confinement energy is larger than the log interaction, the interaction $-\sum_{i>j}\tilde{q}_i\tilde{q}_j \ln(e^\gamma \tilde{r}_{ij}/2)$ is negligible compared with the magnetic confinement energy of each particle. The dimensionless total energy is the sum of the zero-point energies of the individual particles in the quadratic potential plus the constant $c(\tilde{r}_*)$. Hence, at large $\tilde{B} \gg 1$:

$$\tilde{E} = \left(\frac{N_e}{\tilde{m}_e} + \frac{N_h}{\tilde{m}_h}\right)\frac{\tilde{B}}{2} + O(1) + c(\tilde{r}_*) \tag{18}$$

$$\approx \left(\frac{N_e}{\tilde{m}_e} + \frac{N_h}{\tilde{m}_h}\right)\frac{\tilde{B}}{2} + \tilde{E}_{\tilde{B}=0}, \tag{19}$$

since $\tilde{E}_{\tilde{B}=0} \sim c(\tilde{r}_*)$, when $\tilde{r}_*$ is large ($\tilde{r}_* \gg 1$).

For small $\tilde{B} \ll 1$, we use the CoM zero-point energy approximation, Eq. (12), in which we assume the quadratic potential varies on the scale of the complex. Then:

$$\tilde{E} = \frac{\tilde{B}}{2}\sqrt{\frac{N_e/\tilde{m}_e + N_h/\tilde{m}_h}{N_e\tilde{m}_e + N_h\tilde{m}_h}} + \tilde{E}_{\tilde{B}=0}. \tag{20}$$

The total energies for X with $m_e = m_h$ are calculated using the finite-element method implemented in MATHEMATICA [102]. The results are converged by increasing the region size and decreasing the maximum cell size in order to achieve at least six digits of precision. This leads to errors comparable errors to QMC (see Sec. IV B). Subtracting the large-$\tilde{B}$, Eq. (19), from the energy shift of X due to external magnetic fields, results in the logarithmic-like behavior in Fig. 9. This suggests the following formula for the energy shift of a generic charge-carrier complex due to external magnetic field:

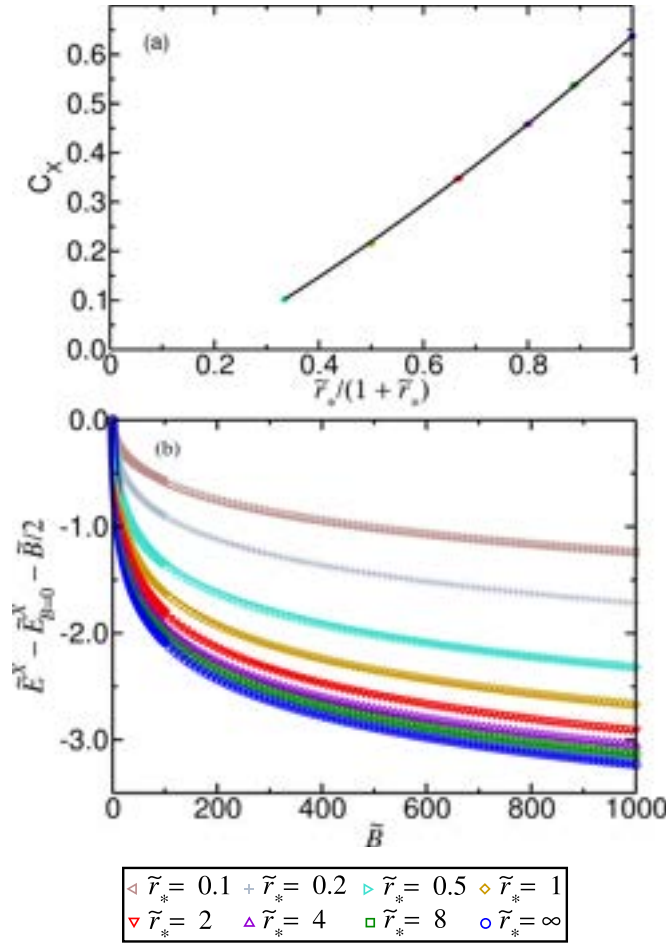

FIG. 9. (a) Dependence of C_X on susceptibility. The markers show fitted C_X. The line is a quadratic fit to the points as for Eq. (22). (b) Shift in energy of X with equal m_e^* and m_h^* due to external magnetic field, after subtracting the large-$\tilde{B}$ behavior from Eq. (19), for several $\tilde{r}_*$. Markers indicate finite-element method results, while lines show the fit of Eq. (21).

$$\tilde{E} - \tilde{E}_{B=0} = \frac{1}{2}\left[\sqrt{\frac{N_e/\tilde{m}_e + N_h/\tilde{m}_h}{N_e\tilde{m}_e + N_h\tilde{m}_h}} - \left(\frac{N_e}{\tilde{m}_e} + \frac{N_h}{\tilde{m}_h}\right)\right]\ln(1 + \tilde{B} + C^2\tilde{B}^2) + \left(\frac{N_e}{\tilde{m}_e} + \frac{N_h}{\tilde{m}_h}\right)\frac{\tilde{B}}{2}, \tag{21}$$

where $C = C(\tilde{r}_*, \sigma)$ is independent of $\tilde{r}_*$ in the $r \ll r_*$ limit in which the logarithmic interaction is valid.

We use the least-squares method to fit the finite-element method results for the BE shift of X with equal m_e^* and m_h^*, Fig. 9, for several values of susceptibility, and extract the

fitting parameter C_X for each $\tilde{r}_*$. We use a polynomial fit to get the dependence of C_X on susceptibility, Fig. 9:

$$C_X = -0.1020(22) + 0.546(9)x + 0.194(6)x^2, \qquad (22)$$

where $x = \tilde{r}_*/(1+\tilde{r}_*)$. Since most 1L-TMDs have effective mass ratios close to 1, Table I, we neglect the mass-ratio dependence of C. Our fit is only valid for $\tilde{r}_* \gtrsim 0.5$. Although the fit from Eq. (21) is derived for the logarithmic interaction, it does fit well our DMC results in Fig. 6 for the full Keldysh interaction for experimentally relevant values, as shown by the red curves in Fig. 6.

ACKNOWLEDGMENTS

We thank M. Aghajanian, A. A. Mostofi, J. Lischner, V. I. Fal'ko, G. Wang for useful discussions. We acknowledge support from EPSRC Grants No. EP/P010180/1, No. EP/L01548X/1, No. EP/K01711X/1, No. EP/K017144/1, No. EP/N010345/1, No. EP/L016087/1, No. EP/X015742/1, No. EP/V000055/1, ERC grants Corr-NEQM (Grant Agreement No. 853368), Hetero2D, GSYNCOR, GIPT, CHARM, Graph-X, Lancaster University's High-End Computing facility, EU Graphene and Quantum Flagship and Graph-X.

[1] C. Ruppert, O. B. Aslan, and T. F. Heinz, Nano Lett. **14**, 6231 (2014).
[2] K. F. Mak, C. Lee, J. Hone, J. Shan, and T. F. Heinz, Phys. Rev. Lett. **105**, 136805 (2010).
[3] A. Splendiani, L. Sun, Y. Zhang, T. Li, J. Kim, C.-Y. Chim, G. Galli, and F. Wang, Nano Lett. **10**, 1271 (2010).
[4] A. Chernikov, T. C. Berkelbach, H. M. Hill, A. Rigosi, L. Albert, Y. Li, B. Aslan, D. R. Reichman, M. S. Hybertsen, and T. F. Heinz, Phys. Rev. Lett. **113**, 076802 (2014).
[5] T. Cheiwchanchamnangij and W. R. L. Lambrecht, Phys. Rev. B **85**, 205302 (2012).
[6] Y. Song and H. Dery, Phys. Rev. Lett. **111**, 026601 (2013).
[7] A. Kormanyos, G. Burkard, M. Gmitra, J. Fabian, V. Zolyomi, N. D. Drummond, and V. I. Fal'ko, 2D Mater. **2**, 022001 (2015).
[8] K. F. Mak, K. He, J. Shan, and T. F. Heinz, Nat. Nanotechnol. **7**, 494 (2012).
[9] H. Zeng, J. Dai, W. Yao, D. Xiao, and X. Cui, Nat. Nanotechnol. **7**, 490 (2012).
[10] X. Xu, W. Yao, D. Xiao, and T. F. Heinz, Nat. Phys. **10**, 343 (2014).
[11] M. Goryca, N. P. Wilson, P. Dey, X. Xu, and S. A. Crooker, Sci. Adv. **5**, eaau4899 (2019).
[12] C. Palacios-Berraquero, M. Barbone, D. M. Kara, X. Chen, I. Goykhman, D. Yoon, A. K. Ott, J. Beitner, K. Watanabe, T. Taniguchi, A. C. Ferrari, and M. Atature, Nat. Commun. **7**, 12978 (2016).
[13] C. Palacios-Berraquero, K. Carmen, M. Dhiren, A. R.-P. Montblanch, M. Barbone, P. Latawiec, D. Yoon, A. K. Ott, M. Loncar, A. C. Ferrari, and M. Atatüre, Nat. Commun. **8**, 15093 (2017).
[14] J. Dang, S. Sun, X. Xie, Y. Yu, K. Peng, C. Qian, S. Wu, F. Song, J. Yang, S. Xiao, L. Yang, Y. Wang, M. A. Rafiq, C. Wang, and X. Xu, npj 2D Mater. Appl. **4**, 2 (2020).
[15] A. R.-P. Montblanch, D. M. Kara, I. Paradisanos, C. M. Purser, M. S. G. Feuer, E. M. Alexeev, L. Stefan, Y. Qin, M. Blei, G. Wang, A. R. Cadore, P. Latawiec, M. Loncar, S. Tongay, A. C. Ferrari, and M. Atatüre, Commun. Phys. **4**, 119 (2021); A. R.-P. Montblanch, M. Barbone, I. Aharonovich, M. Atatüre, A. C. Ferrari, Nat. Nanotechnol. **18**, 555 (2023).
[16] E. E. Salpeter and H. A. Bethe, Phys. Rev. **84**, 1232 (1951).
[17] A. Ramasubramaniam, Phys. Rev. B **86**, 115409 (2012).
[18] C. Robert, R. Picard, D. Lagarde, G. Wang, J. P. Echeverry, F. Cadiz, P. Renucci, A. Hogele, T. Amand, X. Marie, I. C. Gerber, and B. Urbaszek, Phys. Rev. B **94**, 155425 (2016).
[19] K. S. Thygesen, 2D Mater. **4**, 022004 (2017).
[20] R. J. Hunt, M. Szyniszewski, G. I. Prayogo, R. Maezono, and N. D. Drummond, Phys. Rev. B **98**, 075122 (2018).
[21] R. J. Needs, M. D. Towler, N. D. Drummond, P. Lopez Rios, and J. R. Trail, J. Chem. Phys. **152**, 154106 (2020).
[22] B. Stebe, E. Feddi, A. Ainane, and F. Dujardin, Phys. Rev. B **58**, 9926 (1998).
[23] D. Xiao, G. B. Liu, W. Feng, X. Xu, and W. Yao, Phys. Rev. Lett. **108**, 196802 (2012).
[24] N. S. Rytova, Dokl. Akad. Nauk. SSSR **163**, 1118 (1965).
[25] L. V. Keldysh, J. Exp. Theor. Phys. Lett. **29**, 658 (1979).
[26] W. A. Harrison, Phys. Rev. B **31**, 2121 (1985).
[27] K. A. Velizhanin and A. Saxena, Phys. Rev. B **92**, 195305 (2015).
[28] M. Szyniszewski, E. Mostaani, N. D. Drummond, and V. I. Fal'ko, Phys. Rev. B **95**, 081301(R) (2017).
[29] E. Mostaani, M. Szyniszewski, C. H. Price, R. Maezono, M. Danovich, R. J. Hunt, N. D. Drummond, and V. I. Fal'ko, Phys. Rev. B **96**, 075431 (2017).
[30] D. M. Ceperley, Rev. Mod. Phys. **67**, 279 (1995).
[31] C. Kittel, *Introduction to Solid State Physics*, 8th ed. (JWiley, New York, and J. Ziman, 1964).
[32] W. M. C. Foulkes, L. Mitas, R. J. Needs, and G. Rajagopal, Rev. Mod. Phys. **73**, 33 (2001).
[33] M. Barbone, A. R.-P. Montblanch, D. M. Kara, C. Palacios-Berraquero, A. R. Cadore, D. De Fazio, B. Pingault, E. Mostaani, H. Li, B. Chen, K. Watanabe, T. Taniguchi, S. Tongay, G. Wang, A. C. Ferrari, and M. Atature, Nat. Commun. **9**, 3721 (2018).
[34] Z. Ye, L. Waldecker, E. Y. Ma, D. Rhodes, A. Antony, B. Kim, X. Zhang, M. Deng, Y. Jiang, Z. Lu, D. Smirnov, K. Watanabe, T. Taniguchi, J. Hone, and T. F. Heinz, Nat. Commun. **9**, 3718 (2018).
[35] Z. Li, T. Wang, Z. Lu, C. Jin, Y. Chen, Y. Meng, Z. Lian, T. Taniguchi, K. Watanabe, S. Zhang, D. Smirnov, and S. Shi, Nat. Commun. **9**, 3719 (2018).
[36] S. Chen, T. Goldstein, T. Taniguchi, K. Watanabe, and J. Yan, Nat. Commun. **9**, 3717 (2018).
[37] K. Hao, J. F. Specht, P. Nagler, L. Xu, K. Tran, A. Singh, C. K. Dass, C. Schuller, T. Koren, M. Richter, A. Knorr, X. Li, and G. Moody, Nat. Commun. **8**, 15552 (2017).
[38] T. Li, M. Li, Y. Lin, H. Cai, Y. Wu, H. Ding, S. Zhao, N. Pan, and X. Wang, ACS Nano **12**, 4959 (2018).
[39] A. L. Efros, M. Rosen, M. Kuno, M. Nirmal, D. J. Norris, and M. Bawendi, Phys. Rev. B **54**, 4843 (1996).

[40] E. Liu, J. van Baren, C.-T. Liang, T. Taniguchi, K. Watanabe, N. M. Gabor, Y. C. Chang, and C. H. Lui, Phys. Rev. Lett. **124**, 196802 (2020).

[41] M. He, P. Rivera, D. V. Tuan, N. P. Wilson, M. Yang, T. Taniguchi, K. Watanabe, J. Yan, D. G. Mandrus, H. Yu, H. Dery, W. Yao, and X. Xu, Nat. Commun. **11**, 618 (2020).

[42] M. Danovich, V. Zolyomi, and V. I. Fal'ko, Sci. Rep. **7**, 45998 (2017).

[43] G. Wang, C. Robert, M. M. Glazov, F. Cadiz, E. Courtade, T. Amand, D. Lagarde, T. Taniguchi, K. Watanabe, B. Urbaszek, and X. Marie, Phys. Rev. Lett. **119**, 047401 (2017).

[44] D. Y. Qiu, F. H. da Jornada, and S. G. Louie, Phys. Rev. Lett. **111**, 216805 (2013).

[45] H. Dery and Y. Song, Phys. Rev. B **92**, 125431 (2015).

[46] C. Robert, B. Han, P. Kapuscinski, A. Delhomme, C. Faugeras, T. Amand, M. R. Molas, M. Bartos, K. Watanabe, T. Taniguchi, B. Urbaszek, M. Potemski, and X. Marie, Nat. Commun. **11**, 4037 (2020).

[47] P. Kapuscinski, A. Delhomme, D. Vaclavkova, A. O. Slobodeniuk, M. Grzeszczyk, M. Bartos, K. Watanabe, T. Taniguchi, C. Faugeras, and M. Potemski, Commun. Phys. **4**, 186 (2021).

[48] M. Yang, L. Ren, C. Robert, D. VanTuan, L. Lombez, B. Urbaszek, X. Marie, and H. Dery, Phys. Rev. B **105**, 085302 (2022).

[49] M. Selig, G. Berghauser, M. Richter, R. Bratschitsch, A. Knorr, and E. Malic, 2D Mater. **5**, 035017 (2018).

[50] Z. Lu, D. Rhodes, Z. Li, D. V. Tuan, Y. Jiang, J. Ludwig, Z. Jiang, Z. Lian, S.-F. Shi, J. Hone, H. Dery, and D. Smirnov, 2D Mater. **7**, 015017 (2020).

[51] T. Hotta, A. Ueda, S. Higuchi, M. Okada, T. Shimizu, T. Kubo, K. Ueno, T. Taniguchi, K. Watanabe, and R. Kitaura, ACS Nano **15**, 1370 (2021).

[52] S. Z. Uddin, H. Kim, M. Lorenzon, M. Yeh, D.-H. Lien, E. S. Barnard, H. Htoon, A. Weber-Bargioni, and A. Javey, ACS Nano **14**, 13433 (2020).

[53] C. Robert, Nat. Nanotechnol. **13**, 982 (2018).

[54] D. M. Jonas, Annu. Rev. Phys. Chem. **54**, 425 (2003).

[55] A. D. Bristow, D. Karaiskaj, X. Dai, T. Zhang, C. Carlsson, K. R. Hagen, R. Jimenez, and S. T. Cundiff, Rev. Sci. Instrum. **80**, 073108 (2009).

[56] G. Nardin, T. M. Autry, G. Moody, R. Singh, H. Li, and S. T. Cundiff, J. Appl. Phys. **117**, 112804 (2015).

[57] M. Paur, A. J. Molina-Mendoza, R. Bratschitsch, K. Watanabe, T. Taniguchi, and T. Mueller, Nat. Commun. **10**, 1709 (2019).

[58] L. D. Landau and E. M. Lifshitz, *Volume 5 of Course of Theoretical Physics*, Statistical Physics, 3rd Edition (Pergamon, 1976), Chap. III, pp. 79–82.

[59] D. V. Tuan, S.-F. Shi, X. Xu, S. A. Crooker, and H. Dery, Phys. Rev. Lett. **129**, 076801 (2022).

[60] M. Aghajanian, A. A. Mostofi, and J. Lischner, Sci. Rep. **8**, 13611 (2018).

[61] F. A. Rasmussen and K. S. Thygesen, J. Phys. Chem. C **119**, 13169 (2015).

[62] H. Shi, H. Pan, Y.-W. Zhang, and B. I. Yakobson, Phys. Rev. B **87**, 155304 (2013).

[63] A. Kumar and P. Ahluwalia, Phys. B: Condens. Matter **407**, 4627 (2012).

[64] I. Kylänpää and H.-P. Komsa, Phys. Rev. B **92**, 205418 (2015).

[65] T. C. Berkelbach, M. S. Hybertsen, and D. R. Reichman, Phys. Rev. B **88**, 045318 (2013).

[66] N. Lu, C. Zhang, C.-H. Lee, J. P. Oviedo, M. A. T. Nguyen, X. Peng, R. M. Wallace, T. E. Mallouk, J. A. Robinson, J. Wang, K. Cho, and M. J. Kim, J. Phys. Chem. C **120**, 8364 (2016).

[67] D. J. Griffiths, *Introduction to Quantum Mechanics*, 2nd ed. (Cambridge University Press, 2016).

[68] A. C. Ferrari *et al.*, Nanoscale **7**, 4598 (2015).

[69] W. P. Krijnen, Comput. Stat. Data Anal. **21**, 133 (1996).

[70] Download Executable_program.zip file from https://doi.org/10.17863/CAM.87211 and follow the instruction provided in README.txt to run the software.

[71] R. Geick, C. H. Perry, and G. Rupprecht, Phys. Rev. **146**, 543 (1966).

[72] M. F. Plass, W. Fukarek, A. Kolitsch, N. Schell, and W. Moller, Thin Solid Films **305**, 172 (1997).

[73] K.-L. Barth, W. Fukarek, H.-P. Maucher, M. F. Plass, and A. Lunk, Thin Solid Films **313-314**, 697 (1998).

[74] S. L. Rumyantsev, M. E. Levinshtein, A. D. Jackson, S. N. Mohammad, G. L. Harris, M. G. Spencer, and M. Shur, *Properties of Advanced Semiconductor Materials GaN, AlN, InN, BN*, SiC, SiGe, edited by M. E. Levinshtein, S. L. Rumyantsev, and M. S. Shur (John Wiley and Sons New York, NY, 2001) Chap. 4, pp. 67–92.

[75] A. V. Stier, N. P. Wilson, K. A. Velizhanin, J. Kono, X. Xu, and S. A. Crooker, Phys. Rev. Lett. **120**, 057405 (2018).

[76] M. Danovich, D. A. Ruiz-Tijerina, R. J. Hunt, M. Szyniszewski, N. D. Drummond, and V. I. Fal'ko, Phys. Rev. B **97**, 195452 (2018).

[77] H. Dery, Phys. Rev. B **94**, 075421 (2016).

[78] K. Murase, Jpn. J. Appl. Phys. **33**, 1385 (1994).

[79] A. K. Harman, S. Ninomiya, and S. Adachi, J. Appl. Phys. **76**, 8032 (1994).

[80] W. H. Chae, J. D. Cain, E. D. Hanson, A. A. Murthy, and V. P. Dravid, Appl. Phys. Lett. **111**, 143106 (2017).

[81] O. A. Ajayi, J. V. Ardelean, G. D. Shepard, J. Wang, A. Antony, T. Taniguchi, K. Watanabe, T. F. Heinz, S. Strauf, and X.-Y. Zhu, 2D Mater. **4**, 031011 (2017).

[82] S. Shree, A. George, T. Lehnert, C. Neumann, M. Benelajla, C. Robert, X. Marie, K. Watanabe, T. Taniguchi, U. Kaiser, B. Urbaszek, and A. Turchanin, 2D Mater. **7**, 015011 (2019).

[83] X. Liu and M. C. Hersam, Adv. Mater. **30**, 1801586 (2018).

[84] M. Z. Mayers, T. C. Berkelbach, M. S. Hybertsen, and D. R. Reichman, Phys. Rev. B **92**, 161404(R) (2015).

[85] C. J. Umrigar, J. Toulouse, C. Filippi, S. Sorella, and R. G. Hennig, Phys. Rev. Lett. **98**, 110201 (2007).

[86] J. Feng, X. Qian, C.-W. Huang, and J. Li, Nat. Photonics **6**, 866 (2012).

[87] Z. Li, Y. Xiao, Y. Gong, Z. Wang, Y. Kang, S. Zu, P. M. Ajayan, P. Nordlander, and Z. Fang, ACS Nano **9**, 10158 (2015).

[88] Y. Lin, X. Ling, L. Yu, S. Huang, A. L. Hsu, Y.-H. Lee, J. Kong, M. S. Dresselhaus, and T. Palacios, Nano Lett. **14**, 5569 (2014).

[89] R. J. Elliott, Phys. Rev. **124**, 340 (1961).

[90] R. G. Sachs, *The Physics of Time Reversal*, 1st ed. (University of Chicago Press, Chicago, 1987).
[91] M. Van der Donck, M. Zarenia, and F. M. Peeters, Phys. Rev. B **97**, 195408 (2018).
[92] X. Zhang, F. Lou, C. Li, X. Zhang, N. Jia, T. Yu, J. He, B. Zhang, H. Xia, S. Wang, and X. Tao, CrystEngComm **17**, 4026 (2015).
[93] F. Bonaccorso, A. Lombardo, T. Hasan, Z. Sun, L. Colombo, and A. C. Ferrari, Mater. Today **15**, 564 (2012).
[94] D. G. Purdie, N. M. Pugno, T. Taniguchi, K. Watanabe, A. C. Ferrari, and A. Lombardo, Nat. Commun. **9**, 5387 (2018).
[95] K. He, N. Kumar, L. Zhao, Z. Wang, K. F. Mak, H. Zhao, and J. Shan, Phys. Rev. Lett. **113**, 026803 (2014).
[96] J. Reitz, F. Milford, and R. Christy, *Foundations of Electromagnetic Theory* (Pearson/Addison-Wesley, 2009).
[97] N. S. Rytova, Vestn. Mosk. Univ. Fiz. **22**, 30 (1967).
[98] G. B. Arfken, H. J. Weber, and F. E. Harris, *Mathematical Methods for Physicists*, 7th ed. (Academic Press, Boston, 2013).
[99] D. M. Ceperley and B. J. Alder, Phys. Rev. Lett. **45**, 566 (1980).
[100] C. J. Umrigar, K. G. Wilson, and J. W. Wilkins, Phys. Rev. Lett. **60**, 1719 (1988).
[101] N. D. Drummond and R. J. Needs, Phys. Rev. B **72**, 085124 (2005).
[102] Wolfram Research, Inc., Mathematica, Version 11.3, Champaign, Illinois (2018).